Structure and Properties of Semicrystalline−Rubbery Multiblock Copolymers

Chong Min Koo,[†] Marc A. Hillmyer,[‡] and Frank S. Bates*,[†]

Department of Chemical Engineering and Materials Science and Department of Chemistry, University of Minnesota, Minneapolis, Minnesota 55455

Received May 27, 2005; Revised Manuscript Received November 8, 2005

ABSTRACT: Linear $(EP)_n$ multiblock copolymers, with $n = 2$, 4, 6, 8, 10, and 12, containing semicrystalline poly(ethylene) (E) and rubbery poly(ethylene-*alt*-propylene) (P) blocks were prepared by catalytic hydrogenation of poly(1,4-butadiene-*b*-1,4-isoprene)$_n$ block copolymers. These materials were investigated by small- and wide-angle X-ray scattering (SAXS and WAXS), transmission electron microscopy (TEM), and tensile mechanical testing. Microstructure was created during cooling in two ways: melt state ordering followed by E crystallization and crystallization-induced segregation from the disordered melt. Two categories of mechanical performance were identified. A relatively low true stress at break ($\sigma_{T,B} < 85$ MPa) always was correlated with crystallization-induced segregation. A high true stress at break ($\sigma_{T,B} \approx 270$ MPa) was recorded when crystallization occurred within microphase-separated lamellae or when $n \geq 10$ notwithstanding crystallization-induced segregation. These results are interpreted on the basis of the degree of coupling between E crystals, which depends on the mode of ordering. This model is supported by SAXS and WAXS data obtained from shear oriented $(EP)_2$ triblock copolymer and differential scanning calorimetry results collected from all the multiblock copolymers.

Introduction

Thermoplastic elastomers (TPE's) are an important class of synthetic polymers, with applications in textiles, adhesives, roofing and road products, footwear, and many other items of commerce. These materials generally fall into one of two classifications: ABA type triblock copolymers such as poly(styrene-*b*-butadiene-*b*-styrene) (SBS) and poly(styrene-*b*-isoprene-*b*-styrene) (SIS) and segmented $(AB)_n$ multiblock copolymers including polyurethanes and modified polyesters and polyamides.[1−3] TPE's generally are exploited for a suite of adjustable physical properties that include high extensibility, toughness, ease of processing through heating or addition of solvent, and relatively low cost. In all cases, the hard blocks serve as reversible cross-links binding together the elastic segments. Most triblock copolymer TPE's contain glassy hard (A) blocks, usually poly(styrene), and rubbery soft (B) blocks, while the multiblock materials (n is typically greater than 25) frequently are synthesized with relatively short crystalline (or liquid crystalline) hard segments and rubbery soft segments. Perhaps the most successful TPE has been produced by nature in the form of silk, a complex protein with an exquisite array of intra- and intermolecular interactions providing an unmatched combination of extensibility, recoverability, strength, and facile processing.

For several years our research group has been investigating the relationships that govern the structure and properties of synthetic linear block copolymers. We have been correlating overall material responses with block architecture, block physical properties, and the state of microdomain alignment.[4−11] Glassy, rubbery, and semicrystalline blocks have been incorporated pairwise into triblock, pentablock, and higher order sequences, and the resulting materials have been evaluated for flow-induced morphology alignment in the melt state and solid-state mechanical properties as a function of microdomain orientation. This report focuses on compositionally symmetric poly(ethylene-*b*-ethylene-*alt*-propylene)$_n$ or $(EP)_n$ multiblock copolymers, a combination of semicrystalline (E) and rubbery (P) blocks.

The mechanical properties of TPE's have been investigated for nearly four decades. Most studies have focused on glassy/rubbery triblock systems (e.g., SBS and SIS), including the effects of microdomain orientation as first reported by Keller and co-workers in the early 1970s.[12−15] Subsequently, a host of other groups have explored the structure−property relationships of lamellar, cylinder, and sphere forming SBS triblocks using small-angle X-ray scattering (SAXS) and electron microscopy.[16−18] At small strains the mechanical response is controlled by the morphology and state of orientation, while at large strains the microstructure can be disrupted, with grain rotation, buckling, and chevron formation. The vast majority of this work has dealt with glassy hard domains. Semicrystalline multiblocks have received much less attention, due largely to inferior strength.[19−22] Nevertheless, there are compelling reasons to learn more about this class of materials.

Improvements in synthetic polymer chemistry during the past two decades have greatly expanded the list of monomers that can be incorporated into block architectures. Perhaps the most important advances have been realized in the area of Zeigler−Natta polymerization, especially the development of efficient single-site metallocene catalysts, which are capable of copolymerizing almost any combination of α-olefins.[23−25] Block copolymerization of ethylene and propylene is now emerging as a potentially viable commercial process. These and future advances will open many opportunities for product development, most involving combinations of rubbery and semicrystalline polymers. $(EP)_n$ represents an ideal model system for exploring the structure−property relationships that govern this important class of block copolymers.

Experimental Section

Synthesis. Compositionally symmetric multiblock copolymers were synthesized by sequential anionic polymerization of butadiene and isoprene in cyclohexane at 40 °C using a lithium counterion.

[†] Department of Chemical Engineering and Materials Science.
[‡] Department of Chemistry.

10.1021/ma051098a CCC: $33.50
Published on Web 12/27/2005

For each polymerization the overall composition (weight fraction of B) was kept close to $w_B \cong 0.5$. Thus, the poly(1,4-butadiene-*b*-1,4-isoprene-*b*-1,4-butadiene) (BIB) triblock copolymers ($n = 2$) contain B blocks that are half the molecular weight of the central I blocks, while BIBIB pentablocks, and higher order multiblocks, contain equal molecular weight interior blocks and end blocks that are half this molar mass. Alternatively, these compounds may be represented as linear sequences of BI diblocks. For example, a pentablock could be depicted as BIIBBIIB. For simplicity, we will refer to all multiblocks as $(BI)_n$ where the total number of blocks is $n + 1$ and the terminal B blocks have half the molecular weight of the internal B and I blocks to ensure compositional symmetry. Triblocks ($n = 2$) and pentablocks ($n = 4$) were synthesized by sequential addition of three and five aliquots of monomer, respectively, to an initiator solution. This strategy becomes impractical as n increases. Multiblocks with $n = 6$, 8, 10, and 12 were produced by coupling living $(BI)_m^-Li^+$ block copolymers with $m = 3$, 4, 5, and 6 using dibromo-*p*-xylene.

$(BI)_n$ multiblock copolymers were dissolved in cyclohexane and reacted with hydrogen (500 psi) over a porous heterogeneous Pt−Re/SiO_2 catalyst (supplied by the Dow Chemical Co.) at 140 °C. Hydrogenation of the B and I blocks leads to a type of linear low-density poly(ethylene) (E) and poly(ethylene-*alt*-propylene) (P), respectively. We refer to these saturated multiblock copolymers as $(EP)_n$. Greater than 99% saturation efficiency was confirmed by FTIR.

Polymer Characterization. The molecular weight and molecular weight distribution of the $(BI)_n$ polymers were determined by gel permeation chromatography (GPC) using an instrument fitted with three Phenomenx Phenogel columns, a Wyatt Optilab DSP differential refractometer, and a Wyatt Dawn multiangle light scattering detector. The refractive indices of poly(1,4-butadiene) and poly(1,4-isoprene) in THF are nearly indistinguishable; therefore, we used a single average value, $dn/dc = 0.127$ cm^3/g, to determine M_w and M_w/M_n.

^{1}H NMR spectra of the $(BI)_n$ polymers, dissolved in $CDCl_3$, were recorded on a Varian Unity Inova 300 spectrometer. The pulse repetition delay time was set at 10 s to ensure a quantitative interpretation of the integrated resonances for use in establishing the $(BI)_n$ multiblock copolymer compositions and block microstructures.

Wide-Angle X-ray Scattering. Wide-angle X-ray scattering (WAXS) was performed on a Bruker WAXS microdiffractometer. 2D WAXS patterns were collected on a Seimens HI-STAR multiwire area detector with a sample-to-detector distance of 6.0 cm. The X-ray beam (wavelength $\lambda = 0.154$ nm) was monochromated using flat graphite and collimated with two 0.8 mm diameter pinhole slits. Typical WAXS experiments were completed in 1 min.

Small-Angle X-ray Scattering. Small-angle X-ray scattering (SAXS) measurements were conducted on a 6 m laboratory scattering line at the Institute of Technology Characterization Facility at the University of Minnesota. A rotating anode generated $\lambda = 0.154$ nm wavelength X-rays that were filtered through a nickel foil and focused using an Osmics multilayer confocal mirror augmented by three pinhole slits. This instrument is equipped with a HI-STAR multiwire area detector. Additional experiments were conducted at the 5ID-D beamline of the DuPont-Northwestern-Dow (DND-CAT) located at the synchrotron research center located at the Advanced Photon Source (APS), Argonne National Laboratory. A double-crystal monochromator followed by two sets of adjustable slits conditioned the 10 keV X-ray beam ($\lambda = 0.154$ nm), which was directed at the specimens. Scattered X-rays were collected on a MAR-CCD detector containing 2048 × 2048 pixels (78.75 × 78.75 μm^2 pixel size) with a 16-bit intensity scale and a 133 mm diameter circular active area. The sample-to-detector distance was 3 m. SAXS experiments were completed in 30 s to 10 min.

Transmission Electron Microscopy. TEM was performed with a JEOL 1210 instrument operating at 120 keV in the bright field mode. Samples were stained according to established procedures.[4] Briefly, specimens were cryo-microtomed at −100 °C to create a flat surface before immersion in an aqueous RuO_4 solution for at least 10 h. Thin films (50−90 nm) were then cryo-microtomed and collected on copper grids for later TEM analysis.

Table 1. Characterizations of $(BI)_n$ Multiblock Copolymers

polymer		$M_w \times 10^{-3}$	M_w/M_n	w_B[b]	% 1,2 in B	% coupling
tri	$(BI)_2$-1	27	1.03	0.47	8.4	0
	$(BI)_2$-2	35	1.07	0.47	8.4	0
	$(BI)_2$-3	46	1.05	0.47	7.6	0
	$(BI)_2$-4	73	1.04	0.48	8.0	0
	$(BI)_2$-5	103	1.02	0.49	6.6	0
	$(BI)_2$-6	145	1.06	0.49	7.0	0
	$(BI)_2$-7	251	1.06	0.48	8.7	0
	$(BI)_2$-8	372	1.25	0.47	6.9	0
penta	$(BI)_4$-1	50	1.02	0.47	8.9	0
	$(BI)_4$-2	94	1.02	0.49	6.5	0
	$(BI)_4$-3	189	1.06	0.48	6.7	0
hepta	$(BI)_6$-1	140	1.02[a]	0.49	7.0	73
nona	$(BI)_8$-1	161	1.03[a]	0.47	8.5	83
undeca	$(BI)_{10}$-1	216	1.03[a]	0.48	8.5	83
trideca	$(BI)_{12}$-1	240	1.02[a]	0.48	8.0	76

[a] Polydispersity calculated on the basis of main peak. [b] Weight fraction of B blocks in $(BI)_n$.

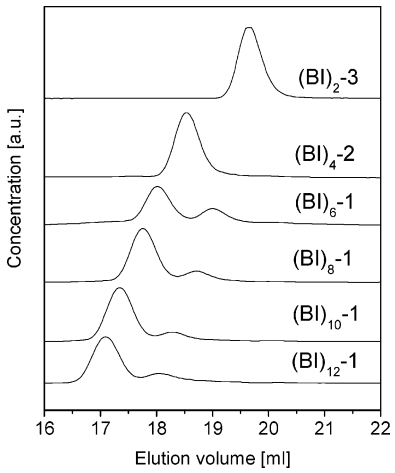

Figure 1. GPC elution curves for $(BI)_n$ in THF at room temperature. These multiblock copolymers are the precursors to the $(EP)_n$ materials. Peaks at higher elution volume ($n = 6$, 8, 10, 12) reflect uncoupled polymer.

Shear Alignment. "Single grain" $(EP)_2$-6 triblock samples were produced using a reciprocating shearing device fitted with a 2 cm × 2 cm by 1 mm thick cell similar to the one described by Koppi et al.[26] A sample was first heated to 124 °C ($T_{ODT} + 10$ °C) while under nitrogen gas and held at that temperature for 10 min. Then the temperature was lowered to 108 °C ($T_{ODT} - 6$ °C), and the material was sheared for 1 h at a shear rate of 0.2 s^{-1} with a strain amplitude of $\gamma = 4$, followed by cooling to room temperature. This procedure (developed by experimenting with numerous combinations of shear rate, strain amplitude, and temperature) results in sheets of well-aligned lamellae (see following section). We will describe the shear alignment behavior of $(EP)_n$ multiblock copolymers in a separate publication.

Mechanical Testing. Tensile deformation experiments (engineering stress $\sigma = F/A_0$ vs engineering strain $\epsilon = (l - l_0)/l_0$, where F = force, A_0 = initial cross-sectional area, l and l_0 = the actual and initial lengths) were carried out at room temperature using a Rheometrics Scientific Minimat instrument operated at a crosshead speed of 5 mm/min. Because of limited sample availability, nonstandard sample dimensions were used: the gage length was 5 mm, gage width 3.15 mm, and thickness 1 mm. Several type V ASTM tensile bars described in the ASTM standard D638 also were used to qualify this testing geometry, and both the standard and nonstandard tensile specimens behaved similarly. A specially designed Minimat sample holder was employed for holding strained samples for SAXS and WAXS testing. This holder allows a tensile

Table 2. Characterizations of $(EP)_n$ Multiblock Copolymers

				DSC		WAXS			SAXS
polymer		$M_w \times 10^{-3}$	w_E	T_m [°C]	$X_{E,DSC}$	a [nm]	b [nm]	$X_{E,WAXS}$	d-spacing [nm]
tri	$(EP)_2$-1	27	0.47	103.4	0.40	0.751	0.499	0.42	27.0
	$(EP)_2$-2	35	0.47	104.4	0.39	0.746	0.495	0.43	28.8
	$(EP)_2$-3	46	0.47	104.4	0.42	0.752	0.498	0.41	30.1
	$(EP)_2$-4	73	0.48	104.5	0.33	0.753	0.501	0.37	34.1
	$(EP)_2$-5	103	0.49	104.3	0.40	0.754	0.501	0.37	36.1
	$(EP)_2$-6	145	0.49	104.5	0.36	0.752	0.497	0.38	45.1
	$(EP)_2$-7	251	0.48	103.8	0.33	0.752	0.496	0.37	64.8
	$(EP)_2$-8	372	0.47	100.9	0.34	0.753	0.499	0.37	80.2
penta	$(EP)_4$-1	50	0.47	102.9	0.36	0.751	0.497	0.40	27.6
	$(EP)_4$-2	94	0.49	103.7	0.36	0.754	0.501	0.37	28.4
	$(EP)_4$-3	189	0.48	101.7	0.33	0.749	0.496	0.38	39.3
hepta	$(EP)_6$-1	140	0.49	101.6	0.33	0.756	0.501	0.32	26.3
nona	$(EP)_8$-1	161	0.47	99.9	0.36	0.753	0.499	0.32	25.6
undeca	$(EP)_{10}$-1	216	0.48	100.3	0.36	0.752	0.499	0.35	19.6
trideca	$(EP)_{12}$-1	240	0.48	97.5	0.38	0.743	0.492	0.38	20.5

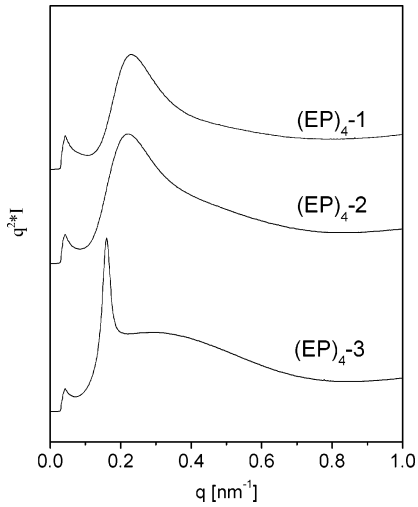

Figure 2. SAXS (synchrotron) patterns of $(EP)_4$ pentablock copolymers at room temperature. The two upper curves have been shifted vertically.

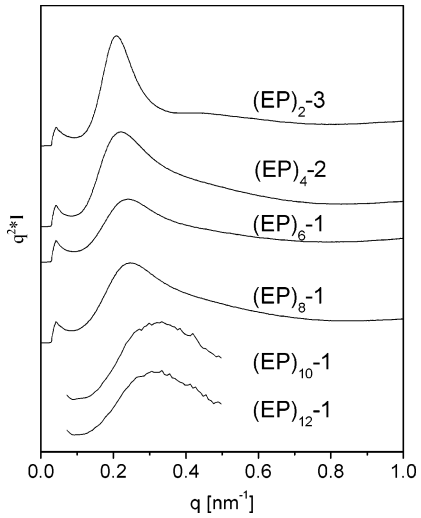

Figure 3. SAXS patterns obtained at room temperature from a series of $(EP)_n$ block copolymers with similar repeating molecular weight, $M_w[(EP)_0] \approx 23$ kg/mol. Curves have been shifted vertically. The upper four traces are synchrotron data while the lower two traces were obtained on the lab instrument.

bar to be removed from the MINIMAT instrument following tensile deformation and mounted in the SAXS or WAXS sample stage while maintaining the state of strain. The total elapsed time between application of strain and acquisition of SAXS or WAXS patterns was about 3−12 min and 3 min, respectively.

Results and Analysis

Synthesis and Molecular Characterization. Table 1 lists the molecular characteristics of 15 different multiblock copolymers: eight triblocks ($n = 2$), three pentablocks ($n = 4$), a heptablock ($n = 6$), a nonablock ($n = 8$), an undecablock ($n = 10$), and a tridecablock ($n = 12$). The triblock and pentablock materials are characterized by monomodal and relatively narrow molecular weight distributions ($M_w/M_n \leq 1.07$). All the higher order multiblocks ($n \geq 6$) displayed a bimodal molecular weight distribution reflecting a combination of coupled and uncoupled polymer. Coupling efficiencies between 73% and 83% are estimated on the basis of relative areas of each peak in the GPC traces recorded for the $(BI)_n$ multiblock copolymers (see Figure 1). These specimens could be fractionated to reduce the amount of uncoupled chains. However, this procedure results in a severe loss of available polymer, which was deemed unacceptable. Moreover, we have shown elsewhere[7] that 80−90% triblock copolymer (CEC) must be added to pentablock copolymer (CECEC) before the fracture behavior is affected qualitatively. In this work we make the assumption that 17−27% of the $n/2$ impurity does not compromise the integrity of this study.

All the B blocks contain between 6.5% and 8.9% 1,2-vinyl segments based on ^{1}H NMR analysis (Table 1) consistent with

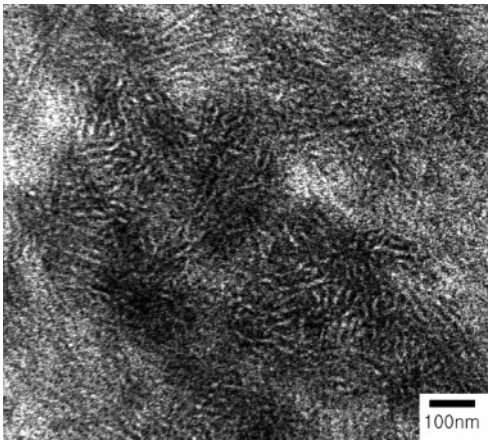

Figure 4. TEM image obtained from a RuO_4 stained thin section of $(EP)_{12}$-1. The light and dark regions correspond to semicrystalline and rubbery domains, respectively.

the polymerization conditions. Hydrogenation converts the B block in these materials into a poly(ethylene-*ran*-ethylethylene) random copolymer, a type of linear low-density poly(ethylene) that we refer to as E. The E block fractional crystallinity ($X_{E,DSC}$) and melting temperature (T_m) were estimated from DSC endotherms obtained while heating as described in a previous publication.[27] Within experimental error all the $(EP)_n$ mutiblocks

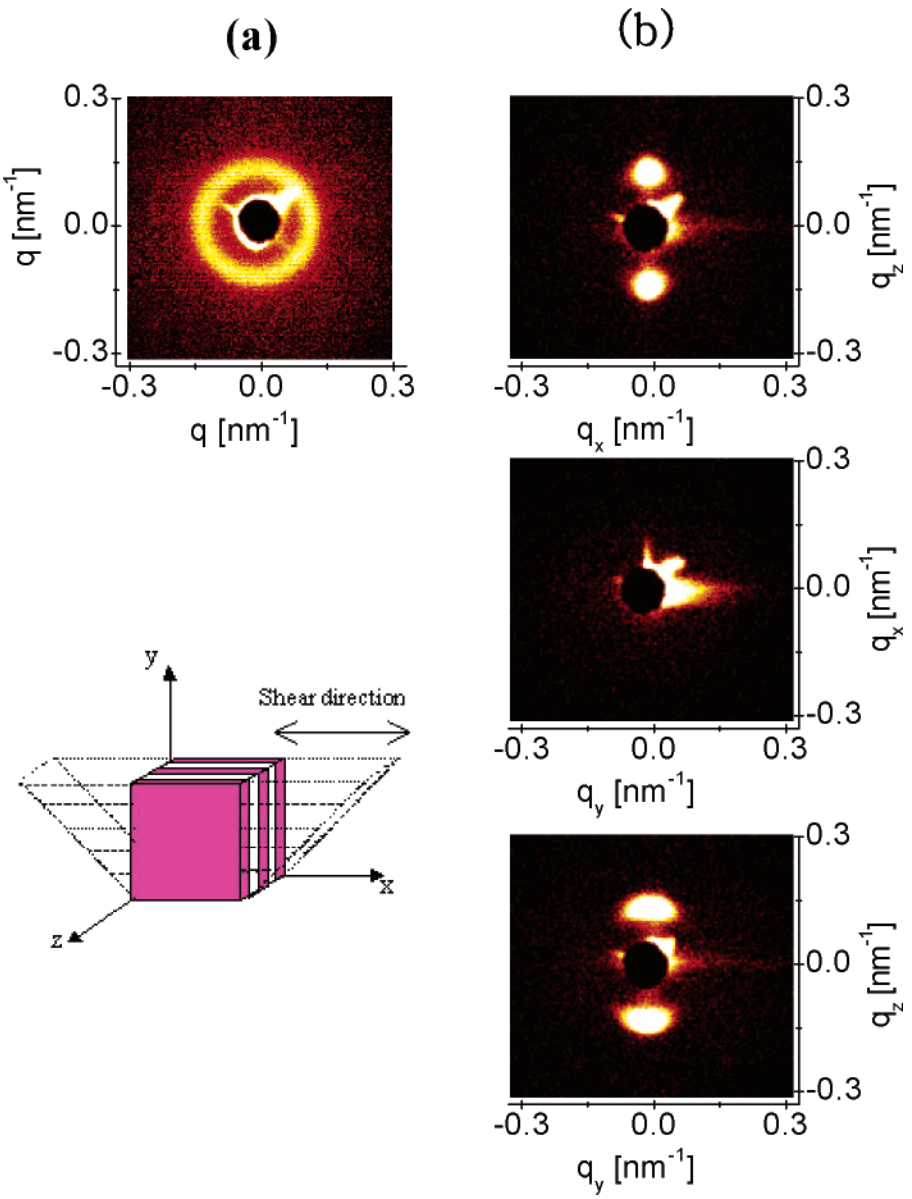

Figure 5. SAXS patterns obtained from (a) unaligned and (b) shear-aligned $(EP)_2$-6 triblock copolymers with the incident beam directed along orthogonal axes at the room temperature. The sketch illustrates the shear geometry: *x*-axis is the shear direction, *y*-axis is the velocity gradient direction, and the *z*-axis is the vorticity direction. Reciprocating shear produced perpendicular alignment of lamellae as indicated in the sketch.

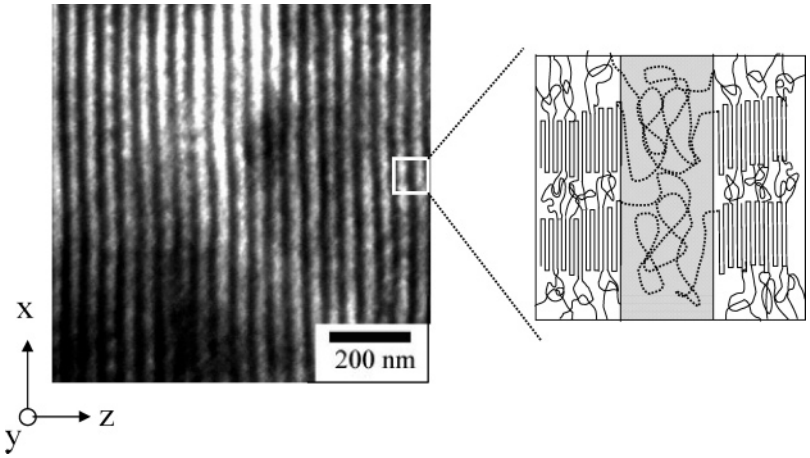

Figure 6. Transmission electron micrograph obtained from shear-aligned $(EP)_2$-6 triblock copolymers and projected onto the $x-z$ plane (see Figure 5). The illustration depicts the state of poly(ethylene) block chain folding within E crystals in ordered and aligned lamellae.

displayed consistent results: $98 \leq T_m \leq 104$ °C and $0.33 \leq X_{E,DSC} \leq 0.42$ (Table 2).

Domain Structural Characterization. None of the multiblock copolymers displayed measurable SAXS intensity above

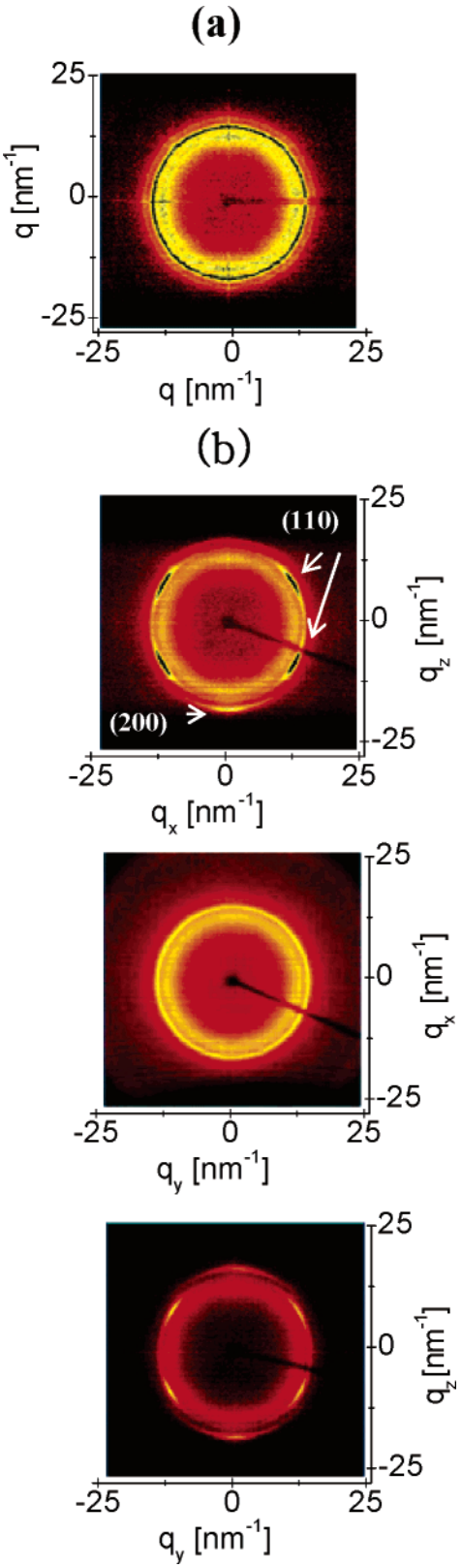

Figure 7. WAXS patterns obtained from (a) unaligned and (b) shear-aligned $(EP)_2$-6 triblock copolymers with the incident beam directed along orthogonal axes at the room temperature; see Figure 5 for scattering geometry.

T_m due to nearly equivalent segment electron densities; poly(ethylene) and poly(ethylene-*alt*-propylene) have almost identical melt densities. Therefore, all SAXS patterns were recorded at room temperature where E block crystallinity creates scattering contrast. Figures 2 and 3 illustrate selected SAXS powder patterns obtained from isotropic specimens that were cooled from the melt state without the application of flow. Figure 2 contains results for the three pentablocks while Figure 3 depicts the SAXS data from a series of six multiblocks ($n = 2$, 4, 6, 8, 10, 12) that share a common core repeat molecular weight, $M_w[(EP)_0] \approx 23$ kg/mol. Peak intensities $I(q^*)$ are associated with a lamellar structure (see below) with periodic spacing $d = 2\pi/q^*$, where $q = 4\pi\lambda^{-1}\sin(\theta/2)$ is the scattering wavevector. Domain dimensions are listed in Table 2. Increasing n at constant $(EP)_0$ leads to a small but systematic reduction in d from 30.1 nm ($n = 2$) to 25.6 nm ($n = 8$) and then a significant drop to 19.6 and 20.5 nm for $n = 10$ and 12, respectively. Figure 4 shows a TEM image of $(EP)_{12}$ in the solid state. A rather fine dispersion of randomly distributed crystallites is apparent, with an average spacing that is consistent with the SAXS determined d value (Table 2). We consider these trends in the Discussion section.

One triblock specimen, $(EP)_2$-6, was further investigated after shear-induced alignment using the recipe outlined in

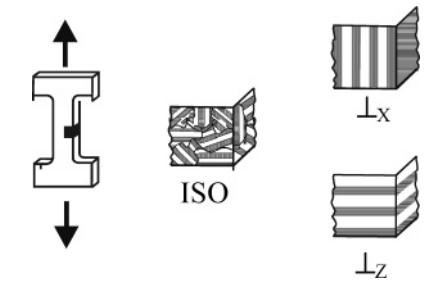

Figure 8. Tensile testing geometry and microdomain orientations for mechanical tests of $(EP)_2$-6 specimens.

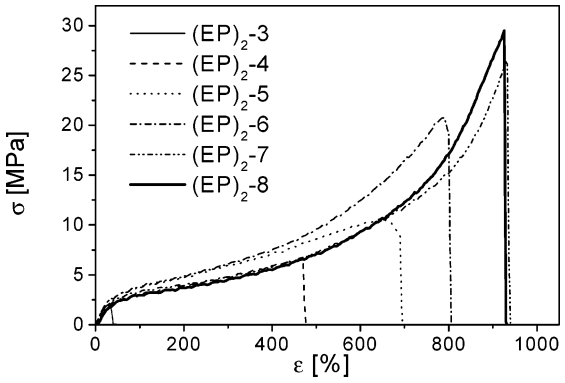

Figure 9. Stress−strain curves from a series of $(EP)_2$ block copolymers with different molecular weights. These data are reproduced from ref 27.

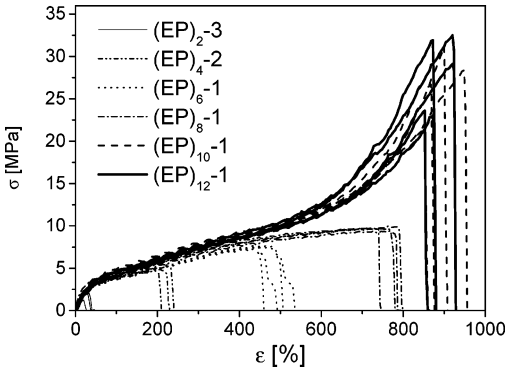

Figure 10. Stress−strain curves of a series of $(EP)_n$ block copolymers with constant core repeat molecular weight, $M_w[(EP)_0] \approx 23$ kg/mol. For $n \leq 8$ the materials strain soften, while for $n \geq 10$ they strain harden.

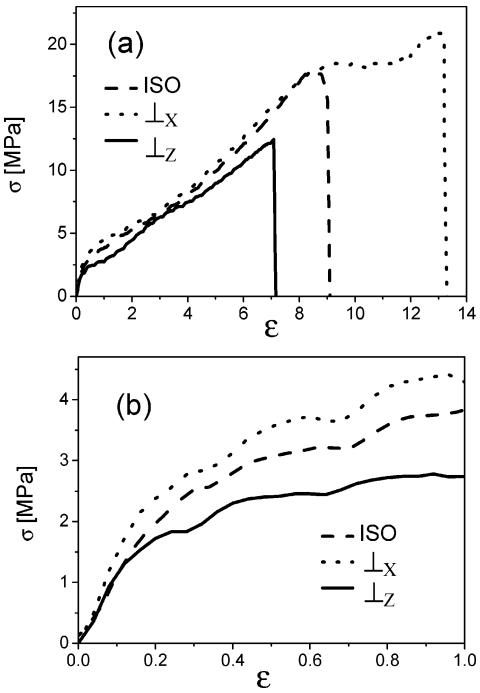

Figure 11. Stress−strain curves for $(EP)_2$-6 samples with three states of alignment (see Figure 8): (a) entire stress−strain curves up to sample failure and (b) expanded plot of the small strain limit.

the Experimental Section. This polymer is characterized by T_{ODT} = 114 °C, providing a narrow temperature window ($T_m < T < T_{ODT}$) within which to operate. Here we note that both the E and P blocks are highly entangled: $M_{e,E}$ = 1 kg/mol and $M_{e,P}$ = 1.5 kg/mol.[28] As a consequence, shear alignment of ordered $(EP)_2$ is rather tricky, requiring relatively low shear rates and limited strain amplitudes. Two-dimensional SAXS patterns taken before and after shearing, with the X-ray beam directed along three orthogonal directions (shear-*x*, vorticity-*z*, and gradient-*y*) are presented in Figure 5. Shearing transforms the initially isotropic morphology into a well-oriented microstructure, with diffraction spots appearing along the scattering wavevector $\mathbf{q}_z$, in both the $\mathbf{q}_x-\mathbf{q}_z$ and $\mathbf{q}_y-\mathbf{q}_z$ scattering planes and absence of scattering in the $\mathbf{q}_x-\mathbf{q}_y$ plane. This specimen was further evaluated by TEM revealing a nearly perfect arrangement of lamellae, as shown in Figure 6, consistent with the SAXS data. Significantly, this "single crystal" specimen contains a state of "perpendicular" alignment as depicted in the sketch in Figure 5. Here we note that our previous publication dealing with $(EP)_2$ triblock copolymers[27] reported a "parallel alignment" following the application of oscillatory shear at a different strain amplitude and deformation rate.

All the higher order multiblocks ($n > 2$) were disordered above T_m on the basis of SAXS and dynamic mechanical spectroscopy measurements (not shown here) and accordingly could not be shear aligned.

Crystal Characterization. WAXS experiments were employed to evaluate the degree of crystallinity in all 15 multiblocks based on powder diffraction and the state of crystal orientation in shear-aligned $(EP)_2$-6. Powder diffraction from all the $(EP)_n$ multiblocks produced similar results that resemble those described in our earlier report.[27] Table 2 lists the associated degrees of crystallinity, $X_{E,WAXS}$, which range from 0.32 to 0.43, i.e., consistent with the DSC results within experimental error. Also, the lattice constants are all consistent with a conventional orthorhombic unit cell.

Shear alignment transforms the cylindrically symmetric WAXS powder patterns, which contain two rings of scattering intensity due to (110) and (200) diffraction, into angularly resolved arcs of intensity in the $\mathbf{q}_x-\mathbf{q}_z$ and $\mathbf{q}_y-\mathbf{q}_z$ scattering planes as shown in Figure 7. These results unambiguously establish that the E block crystals are oriented with stems parallel to the plane of the lamellae as depicted in Figure 6. Thus, crystal

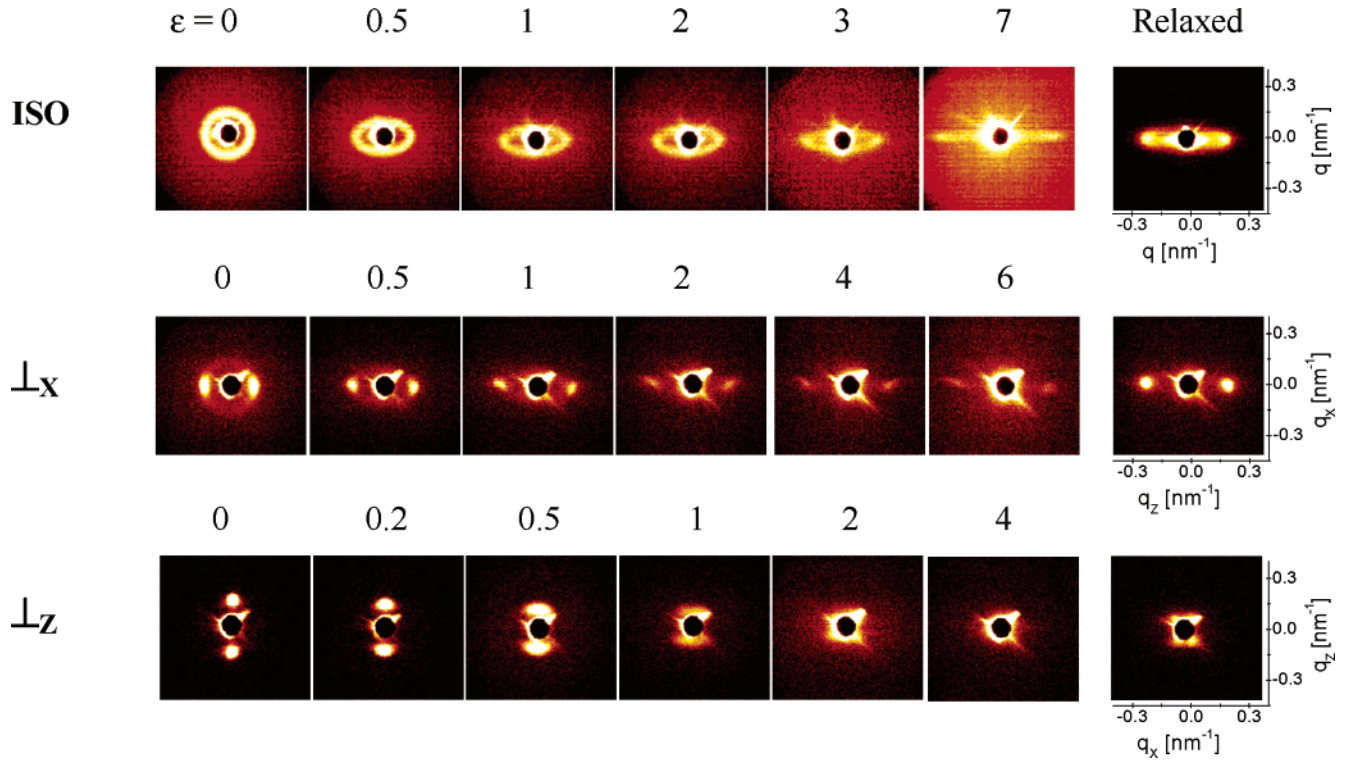

Figure 12. SAXS patterns from $(EP)_2$-6 with three microstructure configurations: (a) ISO, (b) $\perp_X$, and (c) $\perp_Z$. In each case the incident beam was directed perpendicular to the drawing direction at various elongations at room temperature. Strained samples were clamped at the indicated strains and removed from the MINIMAT testing apparatus and oriented in the X-ray beam.

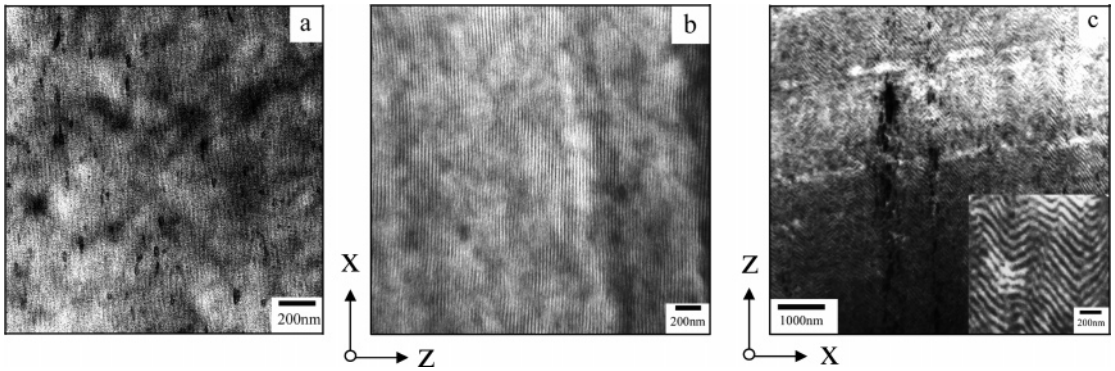

Figure 13. Transmission electron micrographs of $(EP)_2$-6 in three configurations after tensile deformation and unloading to the relaxed state identified in Figure 12: (a) ISO, (b) $\perp_X$, and (c) $\perp_Z$.

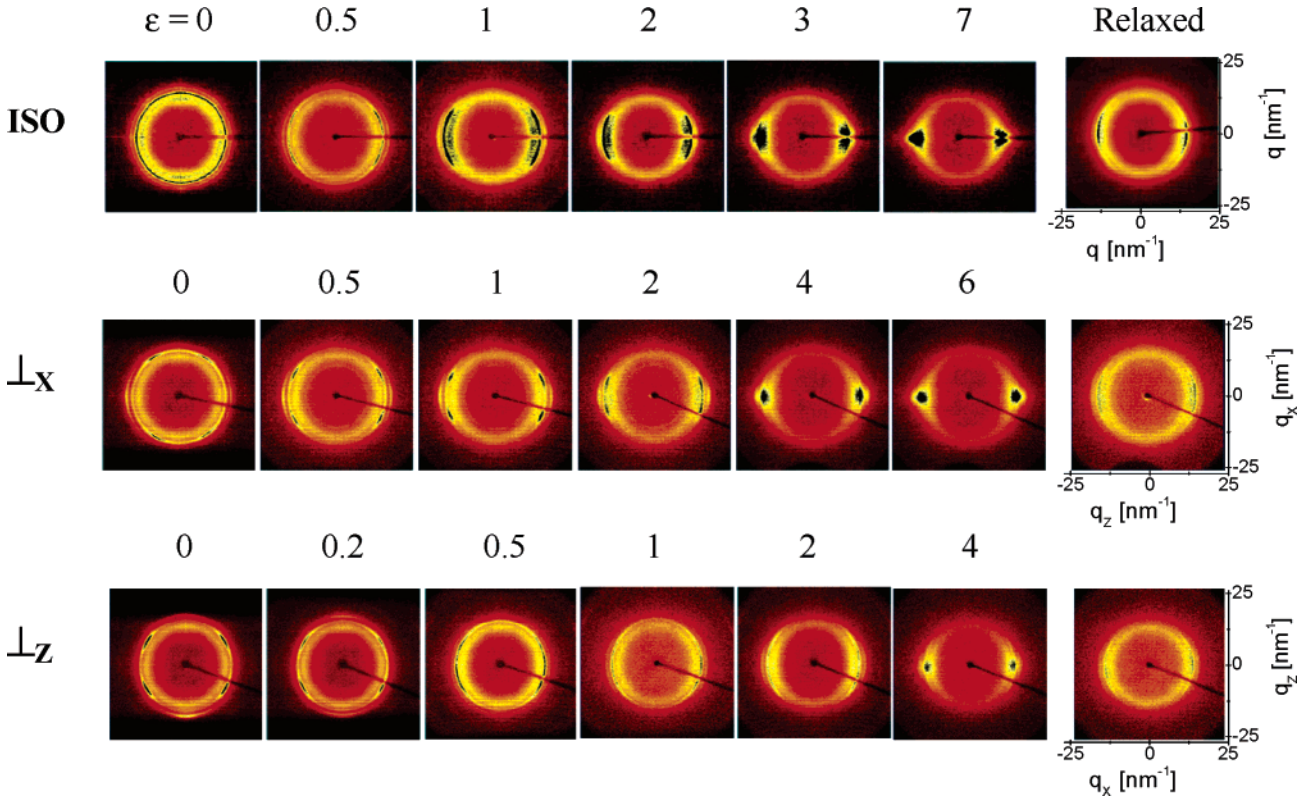

Figure 14. WAXS patterns for the same $(EP)_2$-6 specimens identified in Figure 12: (a) ISO, (b) $\perp_X$, and (c) $\perp_Z$.

orientation within lamellae is independent of the state of shear alignment.[27] (This conclusion is not trivial as the state of bridging and looping conformations has been implicated in the transition from a parallel to perpendicular orientation.[10,11])

We return to both the SAXS and WAXS techniques after describing the stress−strain behavior of the multiblock copolymers.

Mechanical Behavior. Stress−strain measurements were conducted on isotropic and aligned specimens using the tensile geometry, as illustrated in Figure 8. In all cases the specimens deformed uniformly in the gage section, i.e., without necking. All the materials were examined in the isotropic state after cooling from the melt. Previously we reported the evolution of tensile properties with increasing molecular weight for the $(EP)_2$ materials. Figure 9 reproduces six of these results, which will be referred to in the Discussion section. Figure 10 shows how stress and strain develop with increasing block number n for a constant core value $M_w[(EP)_0] \approx 23$ kg/mol; all these multiblocks are disordered above T_m. These reproducible traces demonstrate that strength (stress at failure, σ_B) and strain at break (ϵ_B) vary enormously with n, ranging from $\sigma_B = 2$ MPa and $\epsilon_B = 25\%$ for the triblock ($n = 2$) specimen up to $\sigma_B = 27$ MPa and $\epsilon_B = 900\%$ for the undecablock ($n = 10$) and tridecablock ($n = 12$) specimens. Two qualitatively different regimes characterize the multiblock mechanical response. For $2 \leq n \leq 8$ the materials appear to strain soften prior to failure; i.e., the slope $d\sigma/d\epsilon$ decreases with increasing strain. Conversely, the $n = 10$ and $n = 12$ multiblocks decidedly strain harden at high extension. Similar, although less dramatic, trends can be identified in the series of triblock curves found in Figure 9, where strain softening and strain hardening can be associated with crystallization-induced and block incompatibility-induced microdomain segregation, respectively. We return to these features in the Discussion section.

The consequences of lamellae orientation on mechanical behavior were examined using the shear-aligned $(EP)_2$-6 specimen. A perpendicular alignment affords access to tensile deformation with the strain applied parallel and perpendicular to the plane of the lamellae. We refer to these test geometries as $\perp_x$ and $\perp_z$ where the subscript identifies the direction of strain

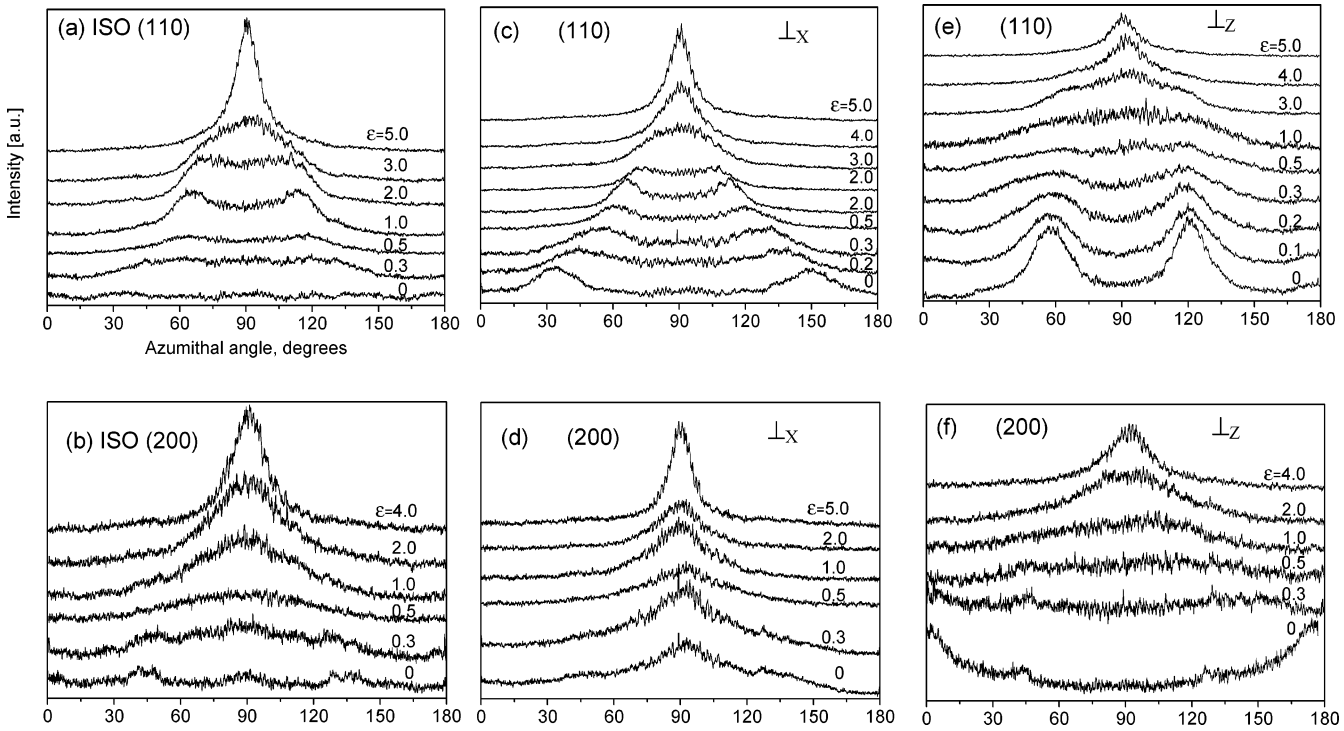

Figure 15. Azumithal intensity profiles extracted from the WAXS data in Figure 14 at scattering wavevector values $q = |\mathbf{q}|$ corresponding to (110) and (200) poly(ethylene) crystal reflections: (a) (110) and (b) (200) in ISO sample; (c) (110) and (d) (200) in $\perp_X$ sample; (e) (110) and (f) (200) in $\perp_Z$ sample.

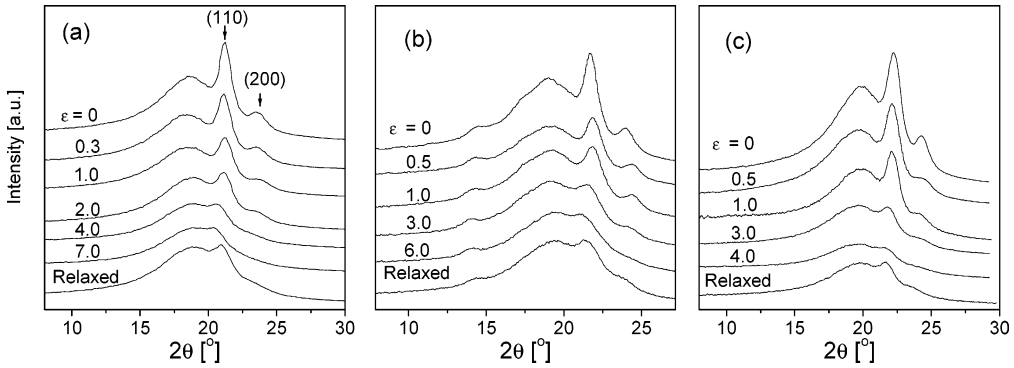

Figure 16. Radial integration of WAXS patterns appearing in Figure 14: (a) ISO, (b) $\perp_X$, and (c) $\perp_Z$ samples at various levels of strain. Loss of the (110) and (200) reflections with increasing strain, and in the relaxed state, signal a transformation from an orthorhombic to fibril crystal form.

according to the coordinate system established during shear orientation (see Figures 5 and 8). Figure 11 compares the stress−strain response obtained from $(EP)_2$-6 in the isotropic, $\perp_x$, and $\perp_z$ arrangements. The highest breaking stress and strain, $\sigma_B = 21$ MPa and $\epsilon_B = 1500\%$, were obtained when the sample was stretched parallel to the plane of the lamellae. Slightly greater than half these values were recorded when the aligned specimen was stretched along the lamellae normal. The isotropic specimen produced intermediate results.

We have documented the changes in microstructure and crystal orientation accompanying these large deformations using SAXS and WAXS measurements. Specimens were clamped at a fixed strain and transferred to the X-ray scattering instruments for measurement. Figure 12 shows three sets of 2-dimensional SAXS patterns illustrating how the microstructure evolves with strain in the isotropic, $\perp_x$, and $\perp_z$ specimens. Drawing the isotropic specimen transforms the initially circular SAXS pattern into an ellipse, with the aspect ratio tracking the macroscopic extension. When $\epsilon = 7$, the minimum d spacing (maximum q^*) is ∼2.5 times the initial value; the maximum d spacing lies beyond the resolution of the SAXS instrument. Stretching in the $\perp_x$ configuration increases q^*; a strain of $\epsilon = 6$ reduces the d spacing to about half the unperturbed dimension. Elongation in the $\perp_z$ configuration produces a more complex sequence of SAXS patterns. Initially, the lamellar period dilates (i.e., the diffraction spots move to smaller $|\mathbf{q}_z|$) up to about 250% strain; then at higher strains a cross pattern appears, indicating reorientation of the microstructure. Releasing the stress leads to partial recovery in lamellar spacing. For example, the unloaded and relaxed $\perp_x$ specimen displays ∼60% of the original d spacing.

TEM images taken from each of the three relaxed specimens referred to in Figure 12 establish the morphological consequences of large strain deformation. The initially isotropic material was transformed into an aligned morphology with a significant reduction in d spacing (Figure 13a). Figure 13b illustrates how stretching in the $\perp_x$ mode preserves a uniform and oriented lamellar morphology while reducing d (compare with Figure 6). Conversely, application of large strains normal to the lamellae ($\perp_z$) leads to irreversible buckling as shown in Figure 13c, which accounts for the diagonal SAXS patterns found in Figure 12.

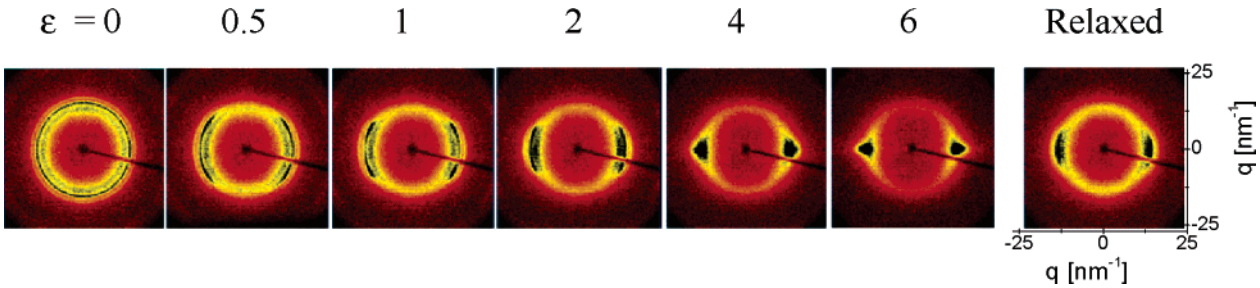

Figure 17. WAXS patterns obtained from isotropic $(EP)_{12}$-1 as a function of tensile strain. These results are nearly indistinguishable from those shown for $(EP)_2$-6 (ISO) in Figure 14.

Three sets of WAXS patterns, taken from the same specimens used to generate the SAXS data shown in Figure 12, are presented in Figure 14. Large strain tensile deformation induces profound changes in chain orientation, evidenced by rotation of the (110) and (200) reflections, beginning with the smallest applied strains (10−30%). These changes are best visualized using azimuthal intensity plots as shown in Figure 15. Lamellae orientation and compression are accompanied by a rearrangement of the crystallites. This process leads to a net loss of crystallinity as revealed by the azimuthally averaged intensity plots shown in Figure 16. Prior to extension all three specimens (isotropic, $\perp_z$, and $\perp_z$) are characterized by well-defined (110) and (200) reflections superimposed on a broad peak due to amorphous scattering. Application of large strains (>400%) nearly eliminates these diffraction peaks, suggesting a transformation of the orthorhombic crystals into a fibril structure.[29−31] This process appears to be mostly irreversible.

All the isotropic specimens that strain harden produced similar WAXS patterns. Figure 17 illustrates this point using $(EP)_{12}$-1. As the strain increases, the initially circular rings of (110) and (200) scattering become focused at poles orthogonal to the direction of strain, reaching nearly instrument resolution spots by $\epsilon = 4$.

Discussion

The results presented in the previous section suggest intriguing correlations among macroscopic tensile deformation, microphase segregation, lamellae orientation, subdomain crystallization, and molecular architecture, in linear semicrystalline/rubbery multiblock copolymers. In this section we establish specific connections between several of these parameters and draw conclusions regarding the factors responsible for the properties exhibited by these soft elastic materials.

Wu and co-workers[10] have shown that the order−disorder transition for compositionally symmetric multiblocks can be closely approximated by the simple linear relationship

$$(\chi N_0)_{ODT} \approx 7.548 + 2.083/n \qquad (1)$$

where N_0 is the degree of polymerization of the repeating diblock unit. For the $(EP)_n$ polymers the Flory−Huggins parameter is given by

$$\chi = 10.3/T - 0.019 \qquad (2)$$

Hence, in the limit $n \rightarrow \infty$ a state of order requires $N_0 > 876$.[32] This explains why all the multiblocks with $n > 2$ are disordered above the E block melting point. Pentablock $(EP)_4$-3 presents an interesting borderline case. Dynamic mechanical spectroscopy measurements (not shown) unambiguously establish a state of disorder at $T > T_m$. However, the SAXS pattern obtained at room temperature (Figure 2) is consistent with crystallization within microphase-separated domains. For this sample $N_0 = 760$, close to the ordering condition. We believe this polymer orders prior to crystallizing during cooling. According to eqs 1 and 2 $T_{ODT} = 75$ °C for this pentablock, well within the range of supercooling within the uncertainties associated with this calculation. We return to this point later in the discussion.

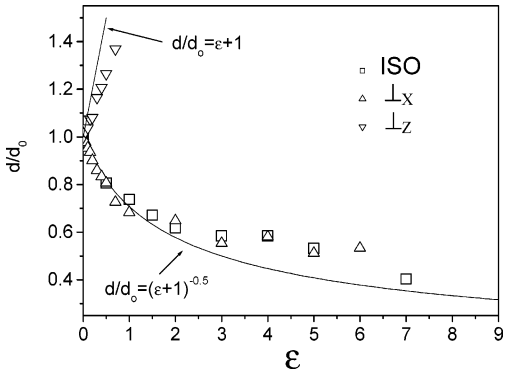

Figure 18. Normalized domain spacing (d/d_0) for $(EP)_2$-6 in the ISO (□), $\perp_X$ (△), and $\perp_Z$ (▽) configurations at various strains. Solid lines indicate affine lateral contraction $(d/d_0 = (\epsilon + 1)^{-0.5})$ and vertical extension $(d/d_0 = (\epsilon + 1))$ of an ideal incompressible network material.

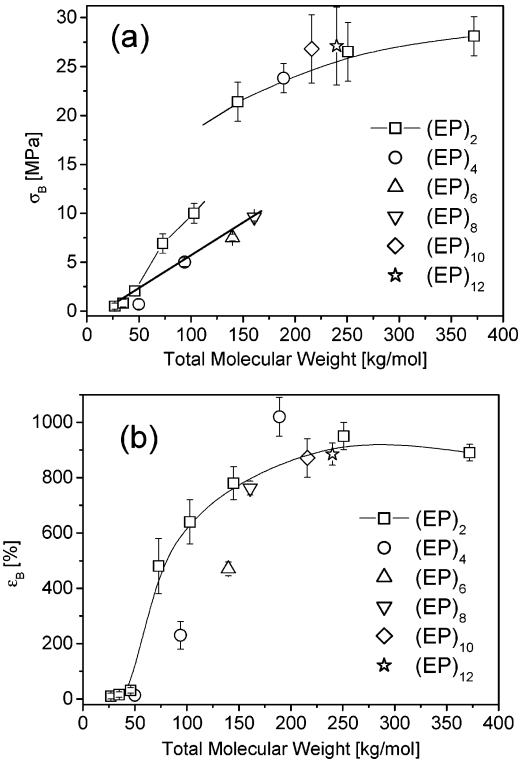

Figure 19. (a) Tensile strength σ_B and (b) elongation at break ϵ_B of $(EP)_n$ block copolymers. The strength results can be classified in two categories: strong, $\sigma_B > 20$ MPa, and weak, $\sigma_B < 10$ MPa. All the specimens in the weak limit are melt disordered and segregate due to crystallization. The strong materials are either melt ordered or characterized by $n \geq 10$.

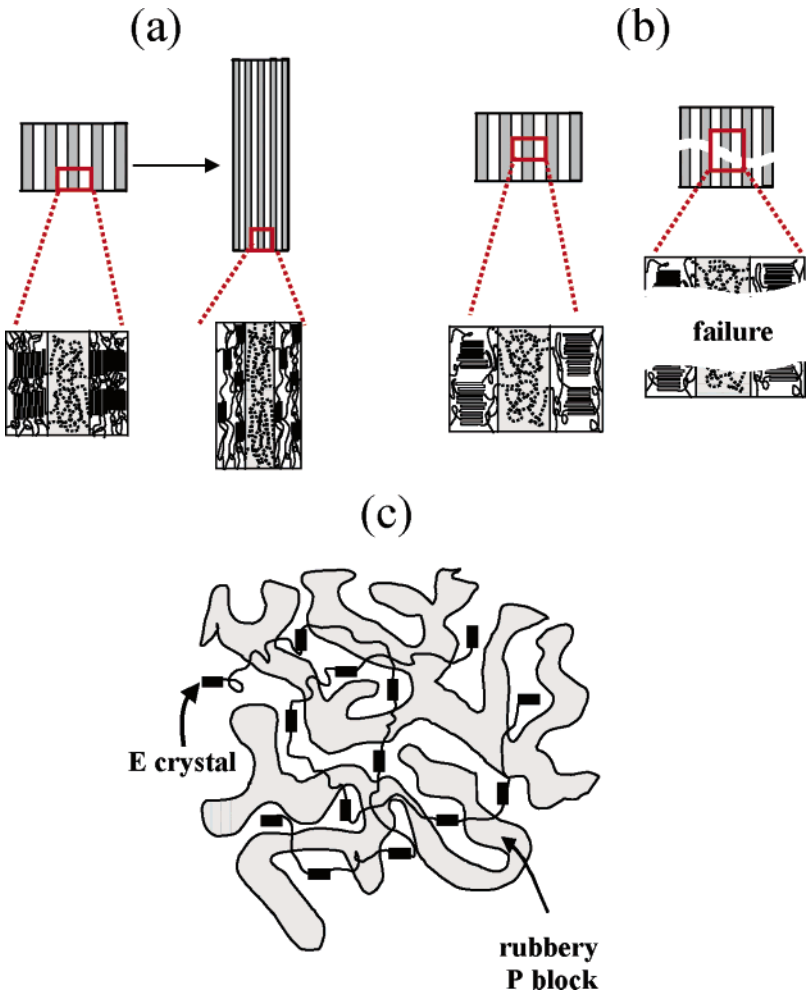

Figure 20. Proposed morphologies and mechanical behavior for $(EP)_n$ multiblock copolymers: (a) melt ordered, (b) crystallization-induced segregation (i.e., melt disordered) with $n < 10$, and (c) homogeneously nucleated and melt disordered multiblocks ($n \geq 10$).

Application of a tensile strain produces nearly affine microstructure deformation in the $\perp_x$ ($d_x/d_0 = (\epsilon + 1)^{-1/2}$) and isotropic ($d_{min}/d_0 = (\epsilon + 1)^{-1/2}$) specimens as illustrated in Figure 18, where $\epsilon = (l - l_0)/l_0$ is the strain. For the $\perp_z$ material the measured d_z/d_0 lags $(\epsilon + 1)$, indicating nonaffine deformation, perhaps anticipating lamellae buckling at about 300% strain. This behavior is reminiscent of the response of semicrystalline/glassy CECEC triblock copolymers ($\perp_z$ geometry), which buckle irreversibly at just 20% strain. Permanent buckling of $(EP)_2$-6 in the $\perp_z$ geometry also is documented in Figure 11.

Perhaps the most intriguing aspect of this work is the transition from strain softening to strain hardening between $n = 8$ and $n = 10$ multiblocks (Figure 10), a trend that mimics melt disordered vs melt ordered triblocks (Figure 9).[27] Average elongation at break and tensile strength are plotted in Figure 19 as a function of total molecular weight (which is proportional to n at constant $M_w[(EP)_0]$) for all the $(EP)_n$ specimens listed in Table 1. Other than a general increase with increasing molecular weight, there is no sensible relationship between ϵ_B and multiblock structure or morphology. However, a clear structure−property relationship emerges from the plot of σ_B vs M_w.

The tensile strength of these materials can be divided into two categories: weak ($\sigma_B < 10$ MPa) and strong ($\sigma_B > 20$ MPa). The strong multiblocks lie on a single universal curve with an asymptotic strength of 27 MPa. The limiting strain at break is about 900%, which translates into a true stress at break of $\sigma_{T,B} \approx 270$ MPa. This value compares favorably with cold drawn CECEC pentablock copolymer, the strongest polyolefin materials we have generated, with $\sigma_{T,B} \approx 320$ MPa.[9] (Because of the glassy C blocks, these plastics can be "cold worked" without significant elastic recovery.) We believe this level of true strength must be associated with load bearing domains of entangled poly(ethylene) crystals. Figures 14−16 evidence massive crystal reorganization during tensile deformation, clearly implicating the E blocks in the strengthening mechanism. Figure 20a provides a sketch illustrating this model. Yet how does this argument account for the high strength exhibited by the disordered undecablock ($n = 10$) and tridecablock ($n = 12$) materials?

Before speculating on this point, we consider the weak materials, which are all disordered. Figure 20b illustrates the postulated morphology for the disordered specimens. Crystallization drives the formation of chain-folded crystals resulting in the development of extended lamellae. Space-filling requirements force the amorphous P blocks to the fold surfaces, between the crystalline layers. This arrangement places the weakest crystal axis perpendicular to the long dimension of the E domains, resulting in poor strength. Unlike the crystals that form within ordered lamellae, these fold surfaces are decoupled by amorphous polymer.

So why does the true strength (i.e., the actual load bearing capability) jump from 85 MPa to nearly 270 MPa when n increases from 8 to 10 (see Figure 19)? Our assessment thus far suggests a transition from decoupled to coupled E crystals, which implies a change in morphology. A 20% drop in d spacing is consistent with this line of reasoning (see Figure 3). While

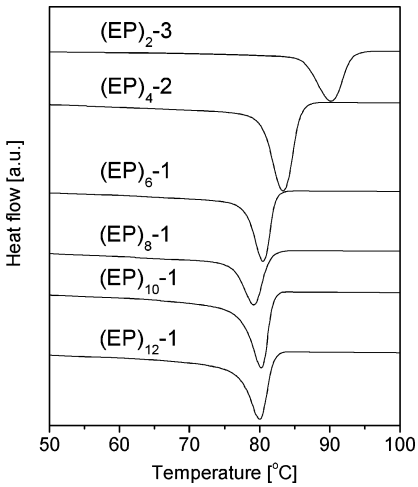

Figure 21. Differential scanning calorimetry (DSC) traces for $(EP)_n$ multiblocks at a constant core repeat size, $M_w[(EP)_0] \approx 23$ kg/mol. Reduction in the crystallization temperature with increasing n indicates a reduced rate of nucleation.

we have no definitive morphological evidence, we speculate that the higher order multiblocks constrain the nucleation and growth of extended lamellar crystals. Obviously, the addition of E blocks to a growing crystal face will be impeded by greater block connectivity, which slows local diffusion and creates conformational restrictions. This may have several consequences. Delayed nucleation would increase the level of supercooling, ultimately resulting in homogeneous nucleation, i.e., spontaneous crystallization throughout the sample. This process, which resembles spinodal decomposition,[33−35] would likely produce a bicontinuous morphology as sketched in Figure 20c. Figure 4, a TEM taken from the undecablock ($n = 12$), is consistent with this notion although we cannot draw any firm conclusions from this image, which suffers from rather low resolution due to limited contrast and a very disorganized morphology. However, DSC experiments, conducted while cooling the $M_w[(EP)_0] \approx 23$ kg/mol multiblocks at 10 °C/min, strongly corroborate the conjecture regarding homogeneous nucleation. Figure 21 reveals increased supercooling as n increases. $(EP)_2$-3 crystallizes at about 90 °C, while $(EP)_4$-2, $(EP)_6$-1, and $(EP)_8$-1 crystallize at 83, 81, and 79 °C, respectively. The largest mutiblocks, $(EP)_{10}$-1 and $(EP)_{12}$-1, appear to order at a limiting value of 80 °C. This asymptotic temperature will be cooling rate dependent; slower cooling will result in a smaller limiting degree of supercooling while faster cooling will produce a larger gap. Hence, the actual limit of homogeneous nucleation will be significantly lower than the 80 °C value evident in Figure 21. Notwithstanding this qualification, these DSC results support our contention that a reduced nucleation rate, and perhaps reduced polymer chain mobility, is responsible for the transition from strain softening to strain hardening as n increases. Moreover, this line of reasoning suggests that the rate at which disordered specimens are cooled could influence the ultimate mechanical behavior.

Conventional multiblock copolymers such as polyurethanes are characterized by the type of disorganized morphology shown in Figure 20c, leading us to speculate that we have accessed the transition from an "oligoblock" to a "multiblock" phase behavior in the $(EP)_n$ system. Based on our model, this transition modifies the coupling mechanism between E crystals to which we attribute a high breaking strength when $n \geq 10$, at the processing conditions applied. Commercial multiblock copolymers, which exhibit high breaking strengths, are almost always in this asymptotic limit ($n \gg 10$) consistent with the present assessment.

Acknowledgment. The authors gratefully acknowledge financial support from Medtronic Corp. and the National Science Foundation (Grant DMR-0220460). Portions of this work were performed at the DuPont−Northwestern−Dow Collaborative Access Team (DND-CAT) Synchrotron Research Center located at Sector 5 of the Advanced Photon Source. DND-CAT is supported by the E.I. DuPont de Nemours & Co., The Dow Chemical Co., and the U.S. National Science Foundation through Grant DMR-9304725 and the State of Illinois through the Department of Commerce and the Board of Higher Education Grant IBHE HECA NWU 96. Use of the Advanced Photon Source was supported by the U.S. Department of Energy, Basic Energy Sciences, Office of Energy Research, under Contract W-31-109-Eng-38. This research also made extensive use of the NSF-MRSEC supported Institute of Technology Characterization Facility at the University of Minnesota, Twin Cities Campus, under Award DMR-0212302.

References and Notes

(1) Holden, G.; Legge, N. R. In *Thermoplastic Elastomers*, 2nd ed.; Hanser Publishers: New York, 1996; pp 48−69.
(2) Quirk, R. P.; Morton, M. In *Thermoplastic Elastomers*, 2nd ed.; Hanser Publishers: New York, 1996; pp 72−100.
(3) Honeker, C. C.; Thomas, E. L. *Chem. Mater.* **1996**, *8*, 1702.
(4) Hermel, T. J.; Wu, L.; Hahn, S. F.; Chaffin, K. A.; Gerberich, W. W.; Bates, F. S. *Macromolecules* **2003**, *36*, 2190.
(5) Bates, F. S.; Fredrickson, G. H.; Hucul, D.; Hahn, S. F. *AIChE J.* **2001**, *47*, 762.
(6) Bates, F. S.; Fredrickson, G. H. *Phys. Today* **1999**, 32.
(7) Mori, Y.; Lim, L. S.; Bates, F. S. *Macromolecules* **2001**, *34*, 951.
(8) Phatak, A.; Macosko, C. W.; Bates, F. S.; Hahn, S. F. *J. Rheol.* **2005**, *49*, 197.
(9) Lim, L. S.; Harada, T.; Hillmyer, M. A.; Bates, F. S. *Macromolecules* **2004**, *37*, 5847.
(10) Wu, L. F.; Cochran, E. W.; Lodge, T. P.; Bates, F. S. *Macromolecules* **2004**, *37*, 3360.
(11) Wu, L. F.; Lodge, T. P.; Bates, F. S. *Macromolecules* **2004**, *37*, 8184.
(12) Keller, A.; Odell, J. A. In *Processing, Structure and Properties of Block Copolymers*; Elsevier Applied Science Publishers: London, 1985; pp 29−74.
(13) Folkes, M. J.; Keller, A. *Polymer* **1971**, *12*, 222.
(14) Odell, J. A.; Keller, A. *Polym. Eng. Sci.* **1977**, *17*, 544.
(15) Arridge, R. G. C.; Folkes, M. J. *J. Phys. D: Appl. Phys.* **1972**, *5*, 344.
(16) Seguela, R.; Prudhome, J. *Macromolecules* **1981**, *14*, 197.
(17) Tarasov, S. G.; Tsvankin, D. Y.; Godovsky, Y. K. *Polym Sci. USSR* **1978**, *20*, 1728.
(18) Pakula, T.; Saijo, K.; Kawai, H.; Hashimoto, T. *Macromolecules* **1985**, *18*, 1294.
(19) Seguela, R.; Prudhome, J. *Polymer* **1989**, *30*, 1446.
(20) Mohajer, Y.; Wilkes, G. L.; Wang, I. C.; McGrath, J. E. *Polymer* **1982**, *23*, 1523.
(21) Falk, J. C.; Schlott, R. J. *Macromolecules* **1971**, *4*, 152.
(22) Falk, J. C.; Schlott, R. J. *Angew. Makromol.* **1972**, *21*, 17.
(23) Gladysz, J. A. *Chem. Rev.* **2000**, *100*, 1167.
(24) Coates, G. W.; Hustad, P. D.; Reinartz, S. *Angew. Chem., Int. Ed.* **2002**, *41*, 2236.
(25) Ruokolainem, J.; Mezzenga, R.; Fredrickson, G. H.; Kramer, E.; Hustad, P. D.; Coates, G. W. *Macromolecules* **2005**, *38*, 851.
(26) Koppi, K. A. Ph.D. Thesis, University of Minnesota, Minneapolis, 1993.
(27) Koo, C. M.; Wu, L.; Lim, L. S.; Mahanthappa, M. K.; Hillmyer, M. A.; Bates, F. S. *Macromolecules* **2005**, *38*, 6090.
(28) Fetters, L. J.; Lohse, D. J.; Richter, D.; Witten, T. A.; Zirkel, A. *Macromolecules* **1994**, *27*, 4639.
(29) Bowden, P. B.; Young, R. J. *J. Mater. Sci.* **1974**, *9*, 2034.
(30) Peterlin, A. *J. Mater. Sci.* **1974**, *9*, 490.
(31) Hinton, T.; Rider, J. G.; Simpson, L A. *J. Mater. Sci.* **1974**, *9*, 1331.
(32) Bates, F. S.; Schulz, M. F.; Rosedale, J. H.; Almdal, K. *Macromolecules* **1992**, *25*, 5547.
(33) White, W. R.; Wiltzius, P. *Phys. Rev. Lett.* **1995**, *75*, 3012.
(34) Jinnai, H.; Koga, T.; Nishikawa, Y.; Hashimoto, T.; Hyde, S. T. *Phys. Rev. Lett.* **1997**, *78*, 2248.
(35) Lauger, J.; Lay, R.; Gronski, W. *J. Phys. Phys.* **1994**, *101*, 7181.

MA051098A